Ballistic transport from propagating vibrational modes in amorphous silicon dioxide: Thermal experiments and atomistic-machine learning modeling

Man Li [a,1], Lingyun Dai [a,1], Huan Wu [a], Yan Yan [b], Joon Sang Kang [a], Sophia King [b], Patricia E. McNeil [c], Danielle Butts [c], Tiphaine Galy [a], Michal Marszewski [a], Esther Lan [c], Bruce S. Dunn [c,d], Sarah H. Tolbert [b,c,d], Laurent Pilon [a,d], Yongjie Hu [a,c,d,e,*]

[a] Department of Mechanical and Aerospace Engineering, University of California, Los Angeles, Los Angeles, CA, 90095, USA
[b] Department of Chemistry and Biochemistry, University of California, Los Angeles, Los Angeles, CA, 90095, USA
[c] Department of Materials Science and Engineering, University of California, Los Angeles, Los Angeles, CA, 90095, USA
[d] California NanoSystems Institute, University of California, Los Angeles, Los Angeles, CA, 90095, USA
[e] Center for Quantum Science and Engineering, University of California, Los Angeles, Los Angeles, CA, 90095, USA

A B S T R A C T

Understanding thermal transport in amorphous materials is critical for a wide range of applications, including buildings, vehicles, aerospace, and acoustic technologies. Despite its importance, the fundamental behavior of heat carriers in amorphous structures remains poorly understood and is often attributed to localized vibrational modes with mean free paths of about 1 nm, posing significant challenges for engineering their thermal functionalities. In this study, we present experimental measurements on mesoporous silica and atomistic analyses using Monte Carlo simulations and machine learning models to quantify the relationship between nanoarchitecture and effective thermal conductivity. Through rational chemical synthesis and ultrafast spectroscopy measurements, a strong size dependence within the sub-10 nm regime is observed, where the classical Fourier heat conduction theory fails to account for the effects of porosity and pore size. This deviation from diffusive transport is attributed to the significant contribution of propagating vibrational modes, in addition to non-propagating modes, revealing unexpectedly long mean free paths and ballistic thermal transport for heat carriers in amorphous silica. The fundamental vibrational modes in amorphous silica are further investigated using spectral-dependent Boltzmann transport equation simulations and molecular dynamics with machine learning potentials, showing good agreement with experimental results. This study provides valuable insights into nanoscale-modulated thermal transport properties in mesoporous silica and opens new opportunities for the rational design of thermally insulating materials.

1. Introduction

Amorphous materials such as silicon dioxide are widely used across various sectors including microelectronics, buildings, automotive, and aerospace [1–3]. Enhancing our understanding of thermal transport in amorphous silica is critical for rational engineering applications [4]. From a computational standpoint, thermal transport in amorphous silica could involve three distinct modes: long-traveling propagons (like phonons), non-propagating diffusons, and localized locons (nearly no contribution to thermal transport) [5–9]. In the literature, early temperature-dependent thermal conductivity measurements have suggested diffusive transport dominates amorphous silica and established the mean free path of heat carriers to be below 1 nm, i.e., almost

non-propagating [10,11]. However, later experimental efforts measuring the thermal conductivity of thermally grown silica films indicated possible longer mean free paths of vibrational modes [12]. Inelastic x-ray scattering experiments also indicate that vibrational modes in amorphous silica can travel up to 10 nm between two consecutive collisions even at temperatures above 1500 K [13,14]. In confined nanoribbons such as $Si/SiO_2/Si$, study also indicates the travel distance of vibrational modes can be longer than 1 nm [15]. These recent studies have stimulated significant interest in exploring non-Fourier transport in amorphous silica [16–26]. Here, we performed direct thermal measurements in mesoporous silica with controlled feature sizes from 20 nm down to 1 nm and discerned the contributions to thermal conductivity from various vibrational modes using atomistic

---

and machine learning assisted modeling analysis. The strategic design of nanoscale architectures in materials has been a crucial approach for modifying thermal properties across diverse applications and for isolating the influences of distinct vibrational modes [27–31].

In this paper, we established synthetic control over mesoporous silica to achieve diverse nanoarchitectures, porosities, and pore sizes, and experimentally measured their effective thermal conductivity, which strongly depends on these structural parameters. Theoretical analyses, combining analytical modeling with machine learning-based molecular dynamics (MD) simulations and Boltzmann transport equation (BTE) calculations, successfully explained the observed variations in thermal conductivity across three distinct nanoarchitectures, which deviate from classical understanding. Notably, the study reveals that vibrational mode scattering induced by nanoscale pores plays a critical role in the unique porosity-dependent thermal conductivity. Furthermore, the combination of experiments and modeling validates the nanoscale interactions between propagating and non-propagating modes, demonstrating a clear distribution of mean free path spectra in the sub-10 nm regime that generate ballistic thermal transport, as observed in these amorphous silicon dioxide samples.

1.1. Mesoporous silica – synthesis and structure

We achieved nanoscale control over mesoporous structures in silicon dioxide through rational synthetic chemistry, and verified with structural characterizations. Specifically, we developed self-assembly processing of surfactant micelles to create templated mesoporous silica, resulting in materials with well-defined ordering and structural forms (see synthesis processes in Supplementary Materials) [32]. As shown in Fig. 1(a), the synthesis approach enables three distinct nanoarchitectures, including: (i) sol-gel-derived and ambiently dried mesoporous silica monoliths (silica ambigels or AM), (ii) sol-gel evaporation-induced self-assembly of block copolymers (used as structure-directing agents) in silica precursors (SG), and (iii) colloidal suspensions of silica nanoparticles (NP).

These resulting nanoarchitectures were verified through structural characterizations. Fig. 1(b) presents a transmission electron microscope (TEM) image of the porous structure of a typical AM sample. The solid framework consists of silica nanoparticles with irregular shapes and diameters of approximately 10 nm, serving as the building blocks. This silica particle network structure was also observed in samples subjected to supercritical drying, leading to silica aerogels.

Fig. 1(c) shows a TEM image of the porous structure of a typical SG sample, where spherical pores are arranged in an orderly manner within the silica matrix. These pores were formed by the removal of uniformly distributed, monodisperse polymer templates upon calcination. Pore size distribution was determined using the Kruk–Jaroniec–Sayari (KJS) method [33], based on low-temperature nitrogen adsorption-desorption isotherms at -196 °C, employing surface area and porosity analyzers (ASAP 2010 and TriStar II 3020, Micromeritics Instrument Corp., Norcross, GA, USA). The average pore diameter was calculated using the Barrett–Joyner–Halenda (BJH) method [34]. The SG samples exhibited pore diameters ranging from 4 nm to 18 nm, with an average diameter of 10 nm.

The porous structure of NP samples was more complex than that of both AM and SG samples. Similar to AM samples, NP samples were constructed from silica nanoparticles; however, the templating polymers introduced additional spherical void spaces within the particulate system. Fig. 1(d) presents a scanning electron microscope (SEM) image of a typical NP sample, highlighting spherical pores with diameters around 10 nm and a branched, polymer-like structure connecting silica nanoparticles. This indicates that NP samples integrated the key features of both SG and AM samples.

1.2. Thermal conductivity of mesoporous silica

The thermal conductivity of mesoporous silica samples was measured using time-domain thermoreflectance (TDTR) technique. TDTR is a standard thermal characterization technique based on ultrafast femtosecond pump-probe optics to provide accurate measurements of thermal conductivity for a variety of materials, including mesoporous silica [35–42]. Our experimental setup is shown in Fig. 2(a) and more
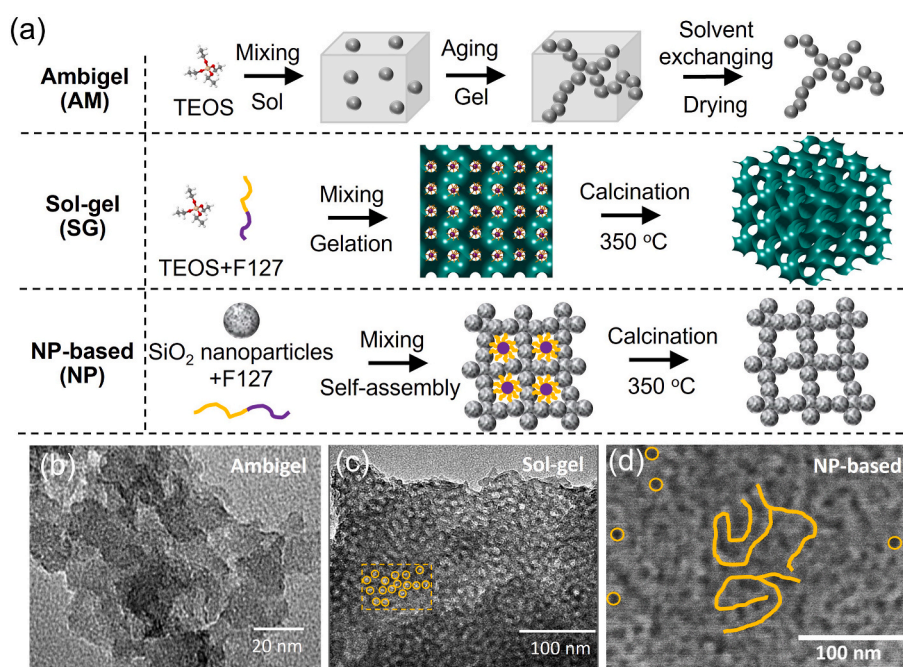
Fig. 1. Chemical synthesis and structural characterizations of mesoporous silicon dioxide films. (a) Synthesis processes of mesoporous SiO₂ ambigel (AM), sol-gel-based mesoporous SiO₂ (SG), and nanoparticle-based mesoporous SiO₂ (NP). (b, c) Typical transmission electron microscope images: (b) the AM sample showing nanosized building blocks and (c) the SG sample displaying ordered pores. (d) A typical scanning electron microscope image of the NP sample illustrating a chain-like network and spherical pores.
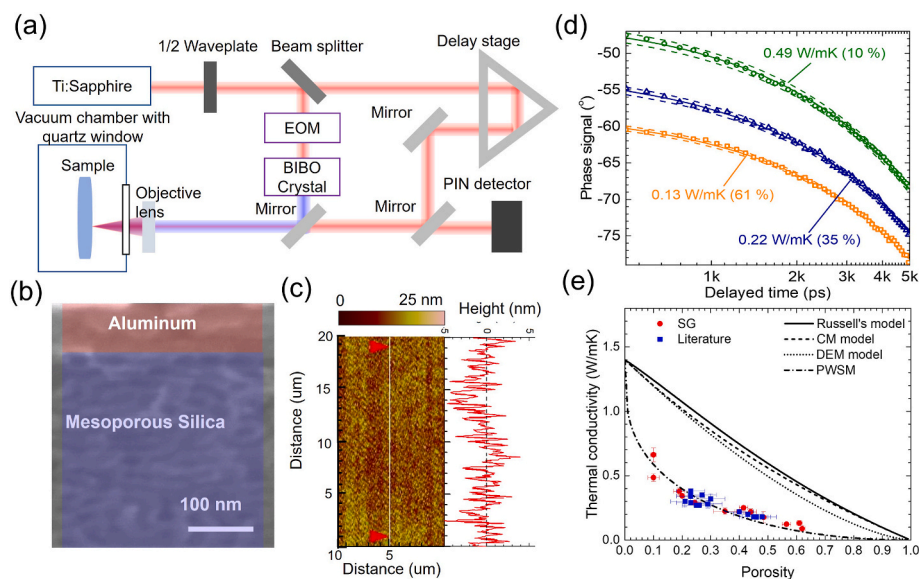
Fig. 2. Thermal conductivity measurements of mesoporous silica. (a) Schematic of the time-domain thermoreflectance (TDTR) setup based on ultrafast optical spectroscopy. (b) Cross-sectional scanning electron microscope image revealing the clear layered structure of the Al/SiO₂ system, required for the layered heat conduction model in TDTR. (c) Atomic force microscope image demonstrating the flatness and uniformity of the sample surface, with a roughness of 2.2 nm. (d) Three representative TDTR datasets from mesoporous samples with varying porosities, along with their best-fitting curves. Dashed lines indicate ±10 % changes in thermal conductivity values. (e) Measured thermal conductivity of SG samples compared with literature values [33] and predicted effective thermal conductivity using various thermal models.

details can be found in our recent reports [35,36,39–42]. A thin aluminum film (~80 nm) was evaporated on the top surface of the samples serving as both a temperature sensor and a transducer converting laser energy to thermal energy. The samples were also characterized to show: (i) the clear interface between Al and sample, (ii) the negligible diffusion of Al into pores, and (iii) the smooth sample surface, as illustrated in the cross-section SEM image of Fig. 2(b). In addition, Fig. 2(c) shows the atomic force microscope image of the sample surface and establishes that the surface roughness of the Al-coated sample was around 2.2 nm, thus fulfilling the flat surface assumption. Fig. 2(d) shows three typical smooth experimental raw datasets with the best curve fit, confirming the validity of the heat conduction model. After the TDTR measurements, the full transient temperature decay curve from 100 to 5000 ps is fitted based on a multi-layered thermal diffusion model to determine the thermal conductivity.

Here, we investigate the effects of the porosity and pore size of these samples on their thermal conductivity. In past literature, porosity has been treated as the sole dominant factor [43,44]. However, here the capability of independent control over the different pore sizes and porosities through the synthesis using varied block-copolymers and polymer-to-TEOS concentrations, enables a comprehensive investigation of effects from the two parameters independently. Ellipsometric porosimetry measurements were performed using toluene as the adsorbate to measure the porosity and pore size distribution of all the samples. The porosity of the AM samples ranged from ~35 % to ~70 %. The porosity of the SG samples varied from ~10 % to ~70 % while that of the NP samples had an upper bound of ~70 % and a lower bound of around 35 %, corresponding to the porosity of close random packing of nanoparticle spheres [45].

We measured thermal conductivity for SG samples with different porosities and plotted in Fig. 2(e). Together, literature data for SG films [44] are usually limited to the range of a much larger porosity; plotted for comparison, they show consistency in the porosity regime. Notably, our measurements show a much stronger dependence on porosity than a simple linear relationship. At a porosity around 50 %, the thermal conductivity decreased to around 0.3 W/mK, corresponding to about 20 % of the thermal conductivity of dense silica (1.4 W/mK) [46]. This was also much lower than the results from these established classical models:

For example, in Fig. 2(e), model results based on Clausius-Mossotti (CM) approximation and the differential effective medium (DEM) approximation are plotted for comparison. As shown, these two classical models significantly overestimate the thermal conductivity of mesoporous silica. We attribute the limitation of the CM and DEM models to their approximation of carrier-level transport details, as well as using spherical cavities in the matrix [43,47,48], which were initially designed for calculating the dielectric constant of composites. Another widely used classical model for thermal conductivity, Russell's model [49,50], was developed based on Fourier's law for porous medium with periodic spherical pores. However, Russell's model was also significantly larger than the measurements. In recent literature, despite a combination fitting method based on series and parallel resistance, such as the porosity-weighted simple model (PWSM) [44] was used to match experiments, it uses weighing factors from empirical fitting and does not provide physical insights. Fundamentally, the discrepancy between the experimental measurements and the classical understanding indicates that possible non-Fourier heat conduction [4] could occur in mesoporous silica, which requires advanced analysis beyond classical models.

1.3. Ballistic thermal transport with varying pore sizes in silica

We further explored both porosity and pore size-dependent thermal transport in all these varying-structured silica samples and observed strong size effects in the sub-10 nm regime, which we attribute to ballistic thermal transport. In literature, size-dependent thermal transport has been mainly studied in crystal materials with relatively long phonon mean free paths [4,28,39,50–54]. However, experimental exploration of the size effects on silicon dioxide has been scarce, because oxides are generally considered to approach the phonon glass limit and thus have extremely small mean free path for local vibrational modes.

Essentially, the thermal transport in mesoporous structures has three channels as illustrated in Fig. 3(a), where gaseous heat conduction and thermal radiation are excluded for our study due to the high vacuum environment and a lower porosity than the threshold for radiation effects to play a non-negligible role [55]. Thus, conduction through solid phases in AM, SC, NP as sketched in Fig. 3(b)–(d), which dominates heat transfer in these structures. Plotted in Fig. 3(e), the direct experimental
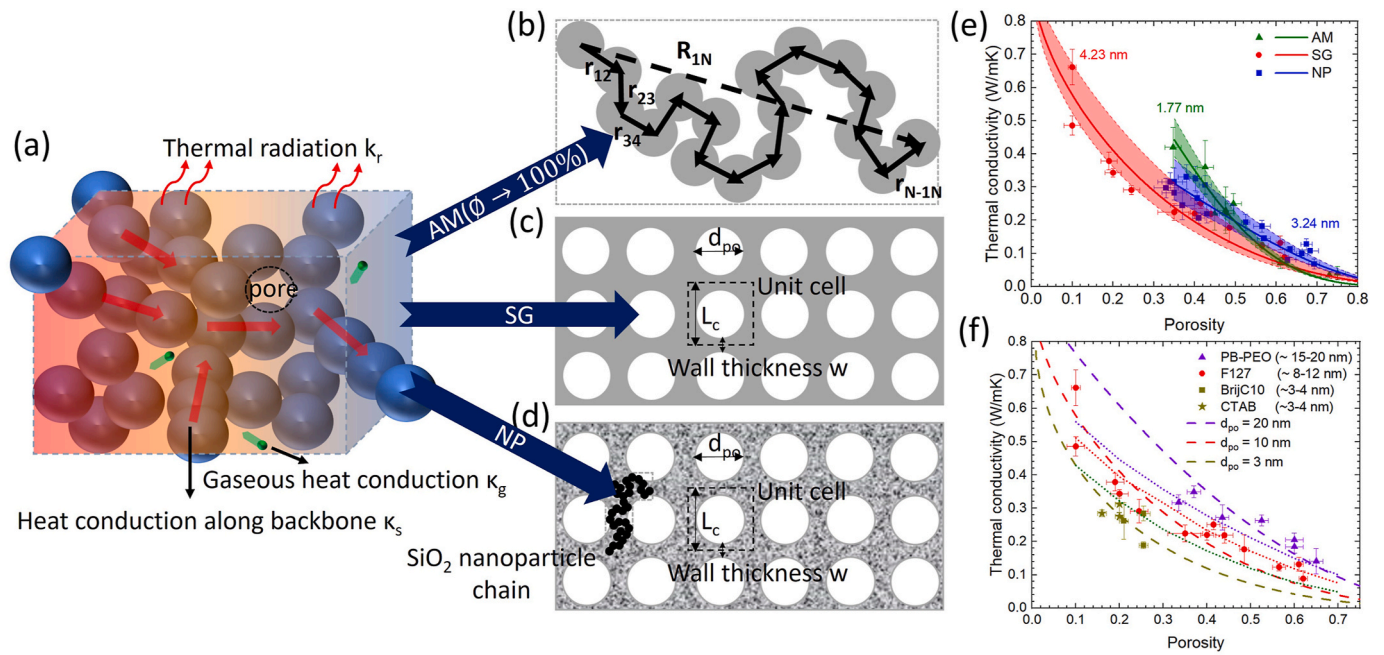
Fig. 3. Analysis of thermal transport in amorphous silicon dioxide, considering propagating and localized vibrational modes. (a) Thermal transport pathways in porous media. (b) Schematic of AM, characterized by extremely high porosity and a polymer-like structure with elongated heat conduction paths due to random bonding between nanoparticles. (c) Schematic of the SG film, featuring an ordered spherical porous structure. (d) Schematic of the NP film, illustrating spherical pores and a pseudo-matrix formed by nanoparticles. (e) Thermal models for three types of mesoporous SiO$_2$: green for AM, red for SG, and blue for NP. The overlapping best-fit solid curves and experimental data demonstrate agreement between the models and the measurements. Shaded regions represent a ± 30 % variation in the mean free path of vibrational modes. (f) SG films prepared with different templating polymers (PB-PEO, Pluronic F127, Brij®C10, and CTAB) exhibit pore sizes of ~20 nm, ~10 nm, ~3 nm, and ~3 nm, respectively. VRMC solved BTE results (dotted line) are plotted with the experimental thermal conductivity values as a function of pore size, together with classical kinetic theory-based model, indicating clear size effects from ballistic thermal transport in sub-10 nm regime.

measurements of the thermal conductivity in all AM, SG and NP silica samples show remarkable dependence on both the porosity and pore size. For total porosity $\phi < 45$ %, AM samples have higher thermal conductivity than NP samples while SG samples have the smallest thermal conductivity. And for porosity >60 %, AM samples have the smallest thermal conductivity. The thermal conductivity of these mesoporous silica samples are then modeled using correction factors accounting for structure porosity and ballistic transport effect on top of the thermal conductivity of dense silica medium (See supplementary materials for modeling details). The model predictions along with the experimental results are shown in Fig. 3(e). Importantly, extracted from all the three models, the average mean free path Λ_D can be up to 4.2 nm, in contrast to the classical perception of ~ 1 nm mean free path for silicon dioxide.

Furthermore, we performed the measurements of thermal conductivity as a function of porosity for SG samples with different pore sizes and found clear size dependence, as unexpected from classical understanding. We prepared SG samples of different pore sizes varying from 2 nm to 25 nm, through the use of different templating polymers. The SG samples made with surfactants CTAB and Brij®C10 typically have very small pores 2–4 nm. In addition, these SG samples are templated with block copolymers PBO-PEO with pore diameters of 15–25 nm. This combination allows tunable structural sizes of the SG samples with highly ordered spherical pores [56]. As shown in Fig. 3(f), the measurement results indicate that the SG films templated with PBO-PEO, present a larger thermal conductivity than those templated with surfactants. The films templated with Pluronic F127 have the second-highest thermal conductivity, followed by films templated with CTAB and Brij®C10. Clearly, under the same porosity, the thermal conductivity decreases with decreasing pore size. This observation contradicts with the classical composite modeling that only porosity (i. e., the relative volume of pores and dense medium) matters to thermal conductivity where the confinement is assumed to be larger than the

intrinsic traveling length of major heat carriers and thus does not play an effective role for thermal transport tunning. Moreover, for the SG samples with 2–4 nm pores, to verify such a conclusion, we repeated the study for samples using two different templating polymers and observed consistent results. Fig. 3(f) also plots three trend lines for the thermal conductivity of SG films with different pore sizes ranging from 3 nm to 20 nm predicted by Eq. (3). The model predictions (dark yellow dashed line) for SG film with a pore size of 5 nm agrees well with the samples prepared with CTAB and Brij®C10. Similarly, the model predictions (violet line) were consistent with thermal conductivity measurements for SG films synthesized by PBO-PEO. The consistency between the experiments and calculations has verified the validation of our analytical modeling and the extracted mean free path of vibrational modes. From these observations, we attribute the size-dependence in the nanostructured silicon dioxide to additional scattering of vibrational modes under limited boundary sizes, i.e., ballistic thermal transport in the sub-10 nm regime.

To quantify such ballistic thermal transport in silicon dioxide and investigate the sub-10nm mean free paths of the vibrational modes, we performed Monte Carlo simulations to solve the three-dimensional spectral Boltzmann transport equation simulation and calculate thermal conductivity of the nanoporous silica systems by adjusting the porosity and pore sizes. Solving the three-dimensional, spectral-dependent Boltzmann transport equation (BTE) using deterministic methods is challenging due to the high dimensionality, complex structures, and spectral dependence. To address these challenges, we apply variance-reduced Monte Carlo (VRMC) algorithm [36,42,46] to efficiently solve the phonon transport in mesoporous structures. In the VRMC algorithm, the behavior of phonon bundles is simulated through 'advection–sampling–scattering' procedures, the spatial temperature distribution is determined by sampling the energy carried by the phonon bundles, and a deviational energy-based technique is employed to enhance computational efficiency. Further details of VRMC approach

can be found in our recent publications [36,42,46] and the supplementary material.

As shown in Fig. 3(f), VRMC solved BTE results are plotted as the dotted lines for porous silica of porosity ranging from 10 % to 70 % and pore size from 20 nm to 5 nm. The geometric structure of porous silica is assumed as one cubic cell, as illustrated in Fig. 3(c) by simplifying the structure observed by SEM in Fig. 1(c). The strong suppression effects of the vibrational modes by the boundary scattering can be observed in the reduction of the effective thermal conductivity with decreasing pore size. The interplay between the experimental measurements and BTE results indicates a clear spreading distribution of the vibrational mean free paths in sub-10 nm regime, which results in the ballistic thermal transport from these traveling modes.

1.4. Machine-learning MD simulations of ballistic transport of vibrational modes

To further provide quantitative analysis on the propagating and localized vibrational modes in amorphous silica requires accurate description for interatomic forces which govern the vibrational dynamics. Herein we performed MD simulations with machine learning potential from quantum mechanical calculations. So far, most atomistic modeling of amorphous silica relies on MD simulations with empirical potential, which were generally derived from measurable bulk material properties, such as density, Young's modulus, and specific heat. With the empirical potentials, these classical MD simulations cannot unambiguously exhibit such size effects as the empirical potentials typically overlook the high-order interactions between atoms, leading to the inaccurate prediction of interatomic forces that drive atomistic dynamics (See Fig. S3). By contrast, density functional theory (DFT) calculations offer a more precise representation of interatomic forces yet are computationally intensive for large supercell sizes. Here, we combined MD simulations with machine learning potential (MLP) trained on DFT calculations, to merge the computational efficiency of MD with the high-fidelity accuracy of DFT [42,57].

We first performed ab initio MD simulations and generated 939 snapshots of mapping between structural configurations and atomic energies, forces, and stresses. The interatomic interactions of liquid and amorphous silica were consequently calculated and shown in Fig. 4(a). The snapshots were divided into a training data set with 750 snapshots and a testing data set with 189 snapshots. The moment tensor potential based on the tensors of inertia of atomistic environments, featuring a balanced accuracy and efficiency, was constructed by machine learning the training data set [58]. To find the MLP parameters, the objective function, defined as the weighted squared error over all energies/forces/stresses between MLP and ab initio MD results, was minimized numerically using Broyden-Fletcher-Goldfarb-Shanno algorithm. The testing root mean squared deviation for energy and forces were 4.5 meV per atom and 123 meV/A, as shown in Fig. 4(b) and (c), indicating significant improvement compared to empirical potentials, for example, BKS and Tersoff potentials (see Fig. S3).

With the MLP, we can generate the amorphous structure of silica by quenching the liquid silica using LAMMPS as shown in Fig. 5(a) [59]. We began with initial structures of β-cristobalite, having a cross-section of 2.8 nm × 2.8 nm and varying thicknesses, and heated them to a liquid phase at 6000 K with a temperature ramping rate of 10 K/ps. The systems were maintained at 6000 K for 20 ps and then quenched to 300 K at a cooling rate of 10 K/ps. After relaxing the systems at 300 K for 10 ps, stable structures of amorphous silica are obtained [60]. The density of the obtained silica is around 2269 kg/m^3, in good agreement with the experimental density of 2220 kg/m^3 [61]. Fig. 5(b) shows good agreement between the radial distribution function of simulated structures with experimental measurements [62]. To evaluate the thickness-dependent thermal conductivity of silica, we introduced a constant heat flux into the system, designating one end as the heat source and the other as the heat sink as in Fig. 5(c) inset on the top. A steady-state linear temperature gradient resulted from this heat flux shown in Fig. 5(c) inset on the bottom. The thermal conductivity was then calculated from the relationship between the heat flux and the temperature profile.
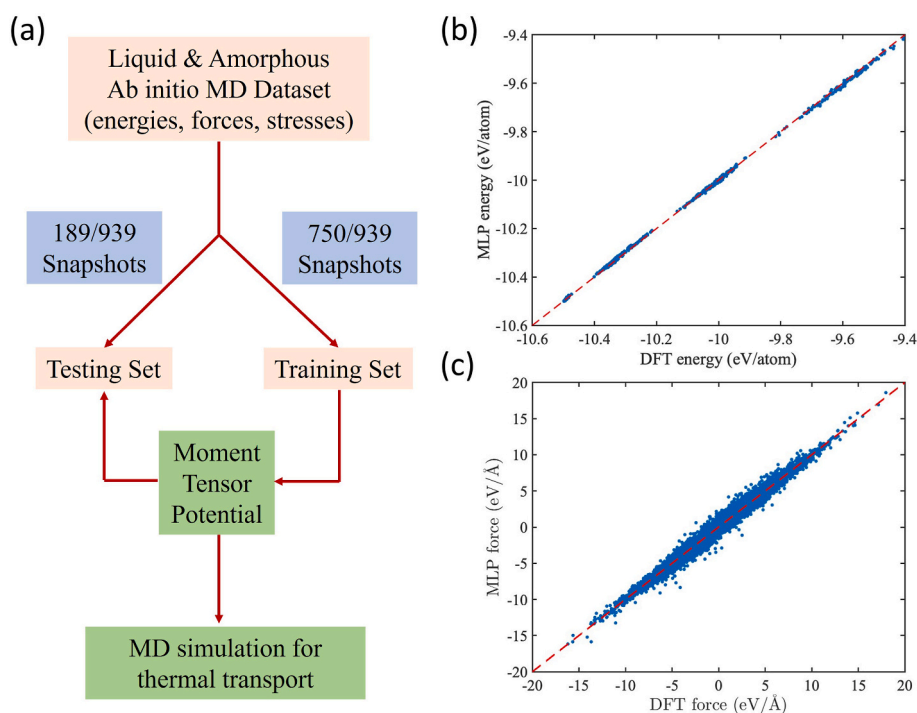
Fig. 4. Machine learning potential for amorphous silicon dioxide. (a) Workflow of the machine learning potential, developed from ab initio molecular dynamics simulations of silica using moment tensor potential. (b, c) Comparison of energy (b) and forces (c) calculated using the moment tensor potential versus those derived from ab initio calculations.
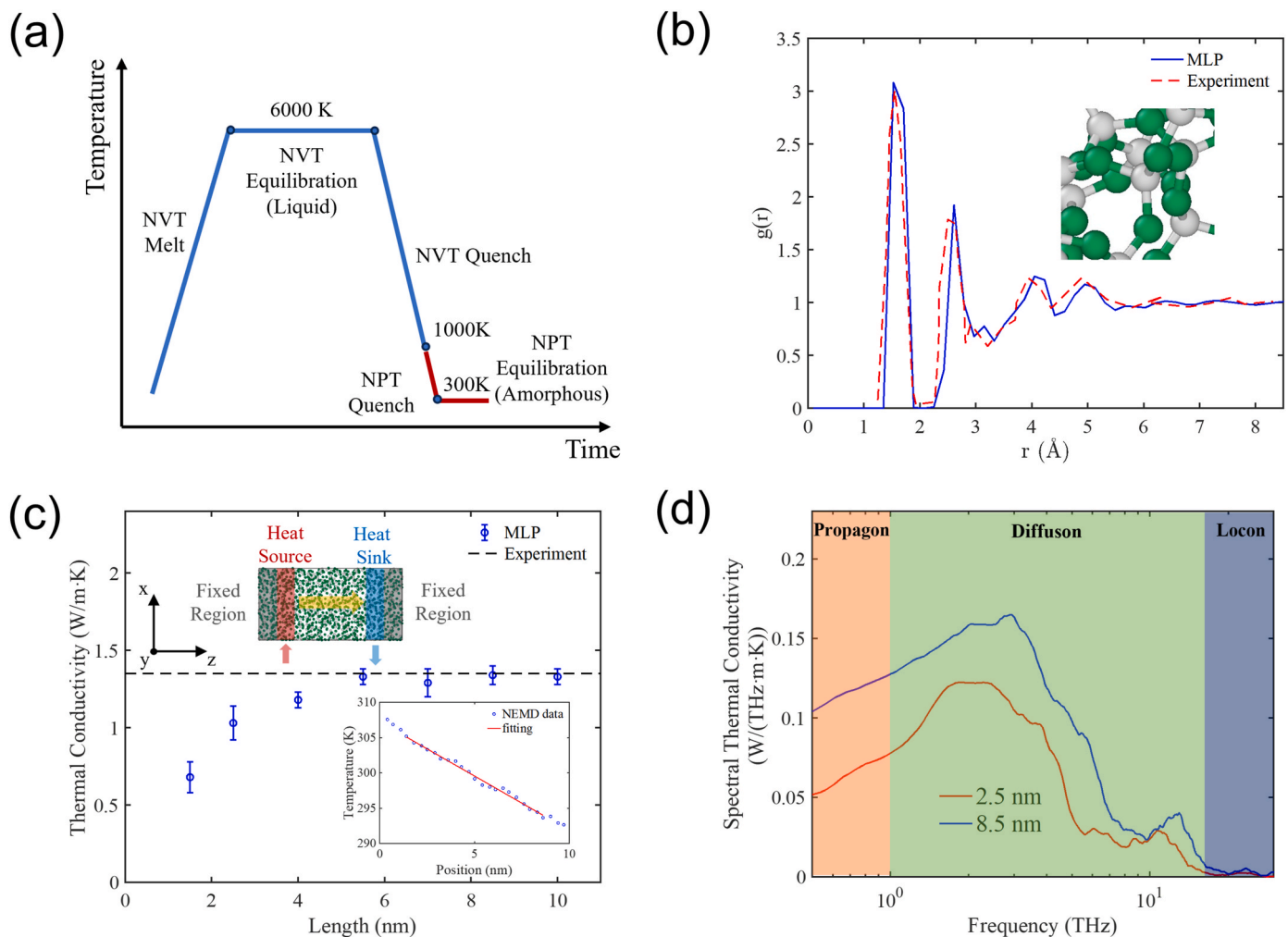
Fig. 5. Ballistic thermal transport from propagating vibrational modes, verified through machine-learning assisted molecular dynamics simulations. (a) Generation of amorphous structures by quenching liquid-phase silica. (b) Radial distribution functions from molecular dynamics simulations; plotted for comparison is experimental data collected through neutron diffraction experiments [52]. (c) Thickness-dependent effective thermal conductivity of silica. The top inset shows the system for non-equilibrium molecular dynamics simulation and the bottom inset shows a representative resulted temperature profile at steady state when a constant heat flux is imposed across the system. (d) The spectral thermal conductivity of amorphous silica, shows mode-dependent contributions from all vibrational modes. The plot exemplifies the results for silica with thickness of 2.5 nm and 8.5 nm, respectively. Vibrational modes inside different frequency regimes are labeled as propagon (red), diffuson (green) and locon (blue).

From this machine learning-assisted MD simulations, we observed a substantial dependence of effective thermal conductivity on thickness less than 5 nm, with values decreasing from approximately 1.35 W/mK to 0.70 W/mK for thickness of 1.5 nm in Fig. 5(c), consistent with experimental results. As expected, the machine learning approach improved interaction potentials and provided more pronounced ballistic effects than empirical MD simulations.

The spectral thermal conductivity can be further obtained by Fourier transform of sampled heat currents involving the velocities of the atoms [63]. This information distinguishes the contribution from all vibrational modes across different frequency, uncovering the fundamental mechanism of vibrational modes behind the phenomenon of size effects. In Fig. 5(d), the spectrum shows as the length of amorphous silica increases from 2.5 to 8.5 nm, both the low-frequency modes (e.g., below 1 THz) and mid-frequency modes (up to 15 THz), have distinctively unlocked potential to contribute to heat conduction. These modes are referred as propagons and diffusons, respectively from the literature [16, 64]. By contrast, the remaining high-frequency modes (or referred to as locons), consistently experience rapid scattering and stay dormant with respect to heat transport, being extremely short-lived due to structural disorder on the level comparable to interatomic distance, regardless of

the reduced boundary effect at a larger scale.

These cross-validation of the collective results from experiments, Monte Carlo BTE and non-empirical MD simulations clearly substantiates the conclusion that there is a spread distribution of mean free paths in silica within the sub-10 nm range.

2. Conclusion

In this work, we studied the propagating and non-propagating vibrational modes in amorphous silicon dioxide, by measuring the structure-dependent thermal transport properties in three distinct types of mesoporous silica with sub-10 nm feature sizes designed through synthetic chemistry. The rational control over nanoscale structures provides a clear dependence of thermal conductivity on both pore sizes and porosity, deviating from classic models. We performed spectral Boltzmann transport equation simulations and molecular dynamics simulations using machine learning potential to quantify ballistic thermal transport in mesoporous silica for the sub-10 nm size regime. The agreement between spectral simulations and experiments verifies that the distribution of mean free paths of propagating and diffusive vibrational modes spread in the sub-10 nm regime with an average value up

to 4.2 nm. The study of ballistic thermal transport established new understanding of thermal transport in amorphous materials and provides fine-size design opportunities for energy sustainability and thermal management systems [27,1,29,65,66].

CRediT authorship contribution statement

Man Li: Writing – review & editing, Writing – original draft, Visualization, Validation, Software, Methodology, Investigation, Formal analysis, Data curation, Conceptualization. **Lingyun Dai:** Writing – review & editing, Writing – original draft, Visualization, Validation, Software, Resources, Methodology, Investigation, Formal analysis, Data curation. **Huan Wu:** Writing – review & editing, Visualization, Validation, Software, Investigation, Formal analysis. **Yan Yan:** Visualization, Validation, Investigation, Formal analysis, Data curation. **Joon Sang Kang:** Validation, Methodology, Investigation, Formal analysis, Data curation. **Sophia King:** Visualization, Validation, Investigation, Formal analysis, Data curation. **Patricia E. McNeil:** Visualization, Validation, Methodology, Investigation, Formal analysis, Data curation. **Danielle Butts:** Visualization, Validation, Methodology, Investigation, Formal analysis, Data curation. **Tiphaine Galy:** Visualization, Validation, Methodology, Investigation, Formal analysis, Data curation. **Michal Marszewski:** Writing – review & editing, Visualization, Validation, Methodology, Investigation, Formal analysis, Data curation. **Esther Lan:** Visualization, Validation, Supervision, Project administration, Investigation, Data curation. **Bruce S. Dunn:** Writing – review & editing, Visualization, Validation, Supervision, Resources, Project administration, Methodology, Investigation, Funding acquisition, Formal analysis, Data curation, Conceptualization. **Sarah H. Tolbert:** Writing – review & editing, Visualization, Validation, Supervision, Resources, Project administration, Methodology, Investigation, Funding acquisition, Formal analysis, Data curation. **Laurent Pilon:** Writing – review & editing, Writing – original draft, Visualization, Validation, Supervision, Resources, Project administration, Methodology, Investigation, Funding acquisition, Formal analysis, Data curation, Conceptualization. **Yongjie Hu:** Writing – review & editing, Writing – original draft, Supervision, Software, Resources, Project administration, Methodology, Investigation, Funding acquisition, Formal analysis, Data curation, Conceptualization.

Declaration of competing interest

The authors declare that they have no known competing financial interests or personal relationships that could have appeared to influence the work reported in this paper.

Acknowledgement

Appendix A. Supplementary data

Supplementary data to this article can be found online at https://doi.org/10.1016/j.mtphys.2025.101659.

Data availability

Data will be made available on request.

References

[1] Z. Qin, M. Li, J. Flohn, Y. Hu, Thermal management materials for energy-efficient and sustainable future buildings, Chem. Commun. 57 (2021): 12236.

[2] C.R. Helms, E.H. Poindexterf, The silicon-silicon-dioxide system: its microstructure and imperfections, Rep. Progr. Phys. 57 (1994) 791.

[3] D.M. Butts, et al., Engineering mesoporous silica for superior optical and thermal properties, MRS Energy and Sustainability 7 (2020) e39.

[4] C. Su, H. Wu, L. Dai, Z. Zhang, S. Li, Y. Hu, Nonclassical heat transfer and recent progress, ASME Journal of Heat and Mass Transfer 147 (2025): 032502.

[5] M.C. Wingert, J. Zheng, S. Kwon, R. Chen, Thermal transport in amorphous materials: a review, Semicond. Sci. Technol. 31 (2016) 113003.

[6] P.B. Allen, J.L. Feldman, Thermal conductivity of disordered harmonic solids, Phys. Rev. B 48 (1993) 12581.

[7] P.B. Allen, J.L. Feldman, J. Fabian, F. Wooten, Diffusons, locons and propagons: character of atomie yibrations in amorphous Si, philosophical magazine B: physics of condensed matter; statistical mechanics, Electronic, Optical and Magnetic Properties 79 (1999) 1715.

[8] W. Lv, A. Henry, Non-negligible contributions to thermal conductivity from localized modes in amorphous silicon dioxide, Sci. Rep. 6 (2016) 35720.

[9] L. Yang, B. Latour, A.J. Minnich, Phonon transmission at crystalline-amorphous interfaces studied using mode-resolved atomistic Green's functions, Phys. Rev. B 97 (2018) 205306.

[10] C. Kittel, Interpretation of the thermal conductivity of glasses, Phys. Rev. 75 (1949) 972.

[11] R.C. Zeller, R.O. Pohl, Thermal conductivity and specific heat of noncrystalline solids, Phys. Rev. B 4 (1971) 2029.

[12] T. Yamane, N. Nagai, S. Katayama, M. Todoki, Measurement of thermal conductivity of silicon dioxide thin films using a 3ω method, J. Appl. Phys. 91 (2002) 9772.

[13] G. Baldi, V.M. Giordano, G. Monaco, B. Ruta, Sound attenuation at terahertz frequencies and the boson peak of vitreous silica, Phys. Rev. Lett. 104 (2010): 195501.

[14] G. Baldi, V.M. Giordano, G. Monaco, B. Ruta, High frequency acoustic attenuation of vitreous silica: new insight from inelastic x-ray scattering, J. Non-Cryst. Solids 357 (2011) 538.

[15] L. Yang, Q. Zhang, Z. Cui, M. Gerboth, Y. Zhao, T.T. Xu, D.G. Walker, D. Li, Ballistic phonon penetration depth in amorphous silicon dioxide, Nano Lett. 17 (2017) 7218.

[16] G. Wei, C. Huang, L. Wang, L. Cui, X. Du, Thermal conductivity modulation mechanism for nanoporous amorphous silica: insights from propagons, diffusons and locons, Int. J. Heat Mass Tran. 240 (2025) 126637.

[17] W.X. Zhou, Y. Cheng, K.Q. Chen, G. Xie, T. Wang, G. Zhang, Thermal conductivity of amorphous materials, Adv. Funct. Mater. 30 (2020) 1903829.

[18] X.K. Chen, Y. Zhang, Q.Q. Luo, P.Z. Jia, W.X. Zhou, Strain-driven anisotropic enhancement in the thermal conductivity of KCaBi: the role of optical phonons, Int. J. Heat Mass Tran. 236 (2025) 126364.

[19] Y. Li, Y. Guo, S. Xiong, H. Yi, Enhanced heat transport in amorphous silicon via microstructure modulation, Int. J. Heat Mass Tran. 222 (2024) 125167.

[20] Y. Xiao, Q. Chen, D. Ma, N. Yang, Q. Hao, Phonon transport within periodic porous structures - from classical phonon size effects to wave effects, ES Mater. Manuf. 5 (2019) 2.

[21] J. Ma, S. Wang, X. Wan, D. Ma, Y. Xiao, Q. Hao, N. Yang, The unrevealed 3D morphological evolution of annealed nanoporous thin films, Nanoscale 14 (2022): 17072.

[22] D. Ma, H. Ding, H. Meng, L. Feng, Y. Wu, J. Shiomi, N. Yang, Nano-cross-junction effect on phonon transport in silicon nanowire cages, Phys. Rev. B 94 (2016) 165434.

[23] Y. He, D. Donadio, G. Galli, Morphology and temperature dependence of the thermal conductivity of nanoporous SiGe, Nano Lett. 11 (2011) 3608.

[24] Y. Liao, S. Iwamoto, M. Sasaki, M. Goto, J. Shiomi, Heat conduction below diffusive limit in amorphous superlattice structures, Nano Energy 84 (2021) 105903.

[25] A. Antidormi, X. Cartoixà, L. Colombo, Nature of microscopic heat carriers in nanoporous silicon, Phys. Rev. Mater. 2 (2018): 056001.

[26] T. Liang, P. Ying, K. Xu, Z. Ye, C. Ling, Z. Fan, J. Xu, Mechanisms of temperature-dependent thermal transport in amorphous silica from machine-learning molecular dynamics, Phys. Rev. B 108 (2023) 184203.

[27] M. Li, H. Wu, E.M. Avery, Z. Qin, D.P. Goronzy, H.D. Nguyen, T. Liu, P.S. Weiss, Y. Hu, Electrically gated molecular thermal switch, Science 382 (2023) 585.

[28] N.A. Rongione, M. Li, H. Wu, H.D. Nguyen, J. Kang, B. Ouyang, H. Xia, Y. Hu, High-performance solution-processable flexible SnSe nanosheet films for lower grade waste heat recovery, Adv. Electr. Mater. 5 (2019) 1800774.

[29] M. Li, Z. Qin, Y. Cui, C. Yang, C. Deng, Y. Wang, J. Kang, H. Xia, Y. Hu, Ultralight and flexible monolithic polymer aerogel with extraordinary thermal insulation by a facile ambient process, Adv. Mater. Interfaces 6 (2019) 1900314.

[30] B. Poudel, et al., High-thermoelectric performance of nanostructured bismuth antimony telluride bulk alloys, Science 320 (2008) 634.

[31] K. Biswas, J. He, I.D. Blum, C.I. Wu, T.P. Hogan, D.N. Seidman, V.P. Dravid, M.G. Kanatzidis, High-performance bulk thermoelectrics with all-scale hierarchical architectures, Nature 489 (2012) 414.

[32] S.H. Tolbert, Mesoporous silica: holey quasicrystals, Nat. Mater. 11 (2012) 749.

[33] M. Kruk, M. Jaroniec, A. Sayari, Application of large pore MCM-41 molecular sieves to improve pore size analysis using nitrogen adsorption measurements, Langmuir 13 (1997) 6267.

[34] E.P. Barrett, L.G. Joyner, P.P. Halenda Vol, R. -RnAtn Apj, R.A. Vn-Rn Atn Ac, The determination of pore volume and area distributions in porous substances, J. Am. Chem. Soc. 73 (1951) 373.

[35] M. Li, J.S. Kang, Y. Hu, Anisotropic thermal conductivity measurement using a new Asymmetric-Beam Time-Domain Thermoreflectance (AB-TDTR) method, Rev. Sci. Instrum. 89 (2018) 084901.

[36] J.S. Kang, H. Wu, Y. Hu, Thermal properties and phonon spectral characterization of synthetic boron phosphide for high thermal conductivity applications, Nano Lett. 17 (2017) 7507.

[37] A.J. Schmidt, X. Chen, G. Chen, Pulse accumulation, radial heat conduction, and anisotropic thermal conductivity in pump-probe transient thermoreflectance, Rev. Sci. Instrum. 79 (2008): 114902.

[38] D.G. Cahill, Analysis of heat flow in layered structures for time-domain thermoreflectance, Rev. Sci. Instrum. 75 (2004) 5119.

[39] J.S. Kang, M. Li, H. Wu, H. Nguyen, Y. Hu, Experimental observation of high thermal conductivity in boron arsenide, Science 361 (2018) 575.

[40] S. Li, Z. Qin, H. Wu, M. Li, M. Kunz, A. Alatas, A. Kavner, Y. Hu, Anomalous thermal transport under high pressure in boron arsenide, Nature 612 (2022) 459.

[41] M. Li, J.S. Kang, H.D. Nguyen, H. Wu, T. Aoki, Y. Hu, Anisotropic thermal boundary resistance across 2D black phosphorus: experiment and atomistic modeling of interfacial energy transport, Adv. Mater. 31 (2019): 1901021.

[42] J.S. Kang, M. Li, H. Wu, H. Nguyen, T. Aoki, Y. Hu, Integration of boron arsenide cooling substrates into gallium nitride devices, Nat Electron 4 (2021) 416.

[43] R.M. Costescu, A.J. Bullen, G. Matamis, K.E. O'Hara, D.G. Cahill, Thermal conductivity and sound velocities of hydrogen-silsesquioxane low-k dielectrics, Phys. Rev. B Condens. Matter 65 (2002): 942051.

[44] T. Coquil, E.K. Richman, N.J. Hutchinson, S.H. Tolbert, L. Pilon, Thermal conductivity of cubic and hexagonal mesoporous silica thin films, J. Appl. Phys. 106 (2009): 034910.

[45] K. Pietrak, T.S. Winiewski, A review of models for effective thermal conductivity of composite materials, Open Access Journal Journal of Power Technologies 95 (2015) 14.

[46] H. Wu, Y. Hu, Ab initio investigations on hydrodynamic phonon transport: From diffusion to convection, Int. J. Heat Mass Transf. 220 (2024) 124988.

[47] E. Talebian, M. Talebian, A general review on the derivation of Clausius-Mossotti relation, Optik 124 (2013) 2324.

[48] A.N. Norris, A.J. Callegari, P. Sheng, A generalized differential effective medium theory, J. Mech. Phys. Solid. 33 (1985) 525.

[49] H.W. Russell, Principles of heat flow in porous insulators, J. Am. Ceram. Soc. 18 (1935) 1.

[50] D. Song, G. Chen, Thermal conductivity of periodic microporous silicon films, Appl. Phys. Lett. 84 (2004) 687.

[51] J. Lee, J. Lim, P. Yang, Ballistic phonon transport in holey silicon, Nano Lett. 15 (2015) 3273.

[52] J.H. Seol, D.S. Barth, J. Zhu, D. Ćoso, K. Hippalgaonkar, J. Lim, J. Han, X. Zhang, A. Majumdar, Tunable thermal conductivity in mesoporous silicon by slight porosity change, Appl. Phys. Lett. 111 (2017) 3164.

[53] J. Tang, H.T. Wang, D.H. Lee, M. Fardy, Z. Huo, T.P. Russell, P. Yang, Holey silicon as an efficient thermoelectric material, Nano Lett. 10 (2010) 4279.

[54] Y. Hu, L. Zeng, A.J. Minnich, M.S. Dresselhaus, G. Chen, Spectral mapping of thermal conductivity through nanoscale ballistic transport, Nat. Nanotechnol. 10 (2015) 701.

[55] L.W. Hrubesh, R.W. Pekala, Thermal properties of organic and inorganic aerogels, J. Mater. Res. 9 (1994) 731.

[56] Y. Yan, M. Li, S. King, T. Galy, M. Marszewski, J.S. Kang, L. Pilon, Y. Hu, S. H. Tolbert, Controlling thermal conductivity in mesoporous silica films using pore size and nanoscale architecture, J. Phys. Chem. Lett. 11 (2020) 3731.

[57] T. Wang, C. Zhang, H. Snoussi, G. Zhang, Machine learning approaches for thermoelectric materials research, Adv. Funct. Mater. 30 (2020): 1906041.

[58] E. Podryabinkin, K. Garifullin, A. Shapeev, I. Novikov, MLIP-3: active learning on atomic environments with moment tensor potentials, J. Chem. Phys. 159 (2023): 084112.

[59] S. Plimpton, LAMMPS-large-scale Atomic/molecular Massively Parallel Simulator, vol. 18, Sandia National Laboratories, 2007, p. 43.

[60] L.C. Erhard, J. Rohrer, K. Albe, V.L. Deringer, A machine-learned interatomic potential for silica and its relation to empirical models, npj Comput. Mater. 8 (2022) 90.

[61] M. Kaviany, Principles of Heat Transfer, Wiley, 2001.

[62] E. Lorch, Neutron diffraction by germania, silica and radiation-damaged silica glasses, J. Phys. C Solid State Phys. 2 (1969) 229.

[63] K. Sääskilahti, J. Oksanen, J. Tulkki, S. Volz, Role of anharmonic phonon scattering in the spectrally decomposed thermal conductance at planar interfaces, Phys. Rev. B Condens. Matter 90 (2014) 134312.

[64] J.M. Larkin, A.J.H. McGaughey, Thermal conductivity accumulation in amorphous silica and amorphous silicon, Phys. Rev. B Condens. Matter 89 (2014).

[65] M. Li, L. Dai, Y. Hu, Machine learning for harnessing thermal energy: from materials discovery to system optimization, ACS Energy Lett. 7 (2022) 3204.

[66] Y. Cui, M. Li, Y. Hu, Emerging interface materials for electronics thermal management: experiments, modeling, and new opportunities, J Mater Chem C Mater 8 (2020): 10568.